Journal of Corrosion and Materials
www.corromat.com

J. Corros. Mater. (2022) 1(2), 93–106.

Calcium-Dependent Oxygen–pH Decoupling at Powder-Processed Fe–Mn–Ag Biodegradable Alloy Interfaces

Kankan Bhattacharyya[1,*], Matteo Ricci[2]

[1] *Department of Chemistry, Indian Institute of Science Education and Research Bhopal, India*
[2] *Department of Mechanical Engineering, Politecnico di Milano, 20156 Milano, Italy.*

[*]Corresponding author: kankan@iiserb.ac.in
[2] riccimatte0it@gmail.com

(Received: 5 August 2022. Received in revised form: 25 October 2022. Accepted: 17 November 2022. Published online: 30 December 2022.)

Abstract

Iron-based biodegradable implants need a corrosive behavior which is more rapid compared to pure Fe and still controlled enough not to induce oxygen deficiency or chemical instability of the surrounding tissue interface. Near-surface pH and dissolved oxygen values have been studied to see whether the near-neutral pH may hide oxygen starvation in powder-processed Fe, Fe35Mn, and (Fe35Mn)5Ag in Hanks' Balanced Salt Solution (HBSS) both without and with addition of calcium salts. The near-surface pH and dissolved oxygen were measured 50 μm away from alloy surface under flowing conditions at 37 °C. The results have been interpreted in connection with the powder-processing technology, composition of the studied alloy and chemistry of the Fe–Mn–Ag system in the electrolyte. pH range, normalized oxygen deficit and oxygen-pH discrepancy ratio are used as criteria of visibility of the interfacial corrosion process. In the calcium-free HBSS (Fe35Mn)5Ag revealed the most pronounced micro-galvanic effects with pH variation of 6.40 to 8.10 and dissolved oxygen drop below 0.50 $mg.L^{-1}$. This case was obviously aggressive as oxygen deficit occurred together with wide pH variations. Different hazard was found in calcium-containing HBSS where early Ca-P precipitates inhibited the oxygen uptake above (Fe35Mn)5Ag but after 24 hours the oxygen minimum dropped to 0.40 $mg.L^{-1}$ whereas pH varied in the range of 7.16 to 7.31. Oxygen-pH discrepancy ratio thus became high indicating that Ca-P precipitation may hide pronounced cathodic oxygen uptake. Fe35Mn alloy demonstrated moderate pH separation but no oxygen uptake inhibition, while pure Fe was sensitive to product-covered oxygen deficiency. The results prove that Fe-Mn-Ag biodegradable alloys cannot be characterized only by corrosion acceleration or pH moderation.

Keywords: biodegradable iron; Fe35Mn; Fe–Mn–Ag; local pH; dissolved oxygen; Hanks' Balanced Salt Solution; calcium phosphate; powder metallurgy.

1. Introduction

For temporary metallic implants, there is a fine balance between being robust enough to maintain structure and functionality throughout the healing process, and being degradable so as not to remain as a permanent foreign body after the end of clinical function. In such regard, biodegradable metallic implants made out of Fe, Zn, and Mg have been proposed as viable alternatives to the more commonly used stainless steels, cobalt-chromium or titanium implants. Long-term in vivo implantation of a corrodible Fe stent has shown persistence of iron-based support within tissues [1]. Pure Fe was subsequently tested for its feasibility as a degradable stent material via in vitro degradation and cell-viability experiments [2]. Studies on biocorrosion and biocompatibility of the material confirmed the potential use of pure Fe as a biodegradable metal [3]. Reviews on biodegradable metallic implants show that Mg and Zn-based alloys along with Fe-based metals have been researched as possible candidates while highlighting the relatively low corrosion rate of the latter two types [4]. As the case with Fe-based alloys, mechanical properties of such metals are superior compared to other metals, yet their relatively slower degradation process poses limitations for vascular stents, fixation elements, and bone substitutes that need to be progressively removed from the body. One of the crucial questions in the design of Fe-based biodegradable implants is how to increase the corrosion rate of Fe without making the local environment toxic for tissues.

The major issue in the use of pure Fe is the presence of the metallic material itself along with corrosion products. Long-term animal experiments of a corrodible Fe stent demonstrated that the material has the tendency to persist longer than desired [1]. In vivo osteosynthesis studies of Fe-based implants also showed slow degradation and persistence of metallic Fe after prolonged implantation periods [5]. This is unlike Mg-based implants, where rapid corrosion along with the production of hydrogen might be the major concerns [6]. The history of biodegradable magnesium implants shows the need for controlling the degradation process [7]. For example, Mg-Zn-Ca metallic glasses have been used as an approach to reduce the amount of observed hydrogen production [8]. Further studies on biodegradable Mg alloys also highlight the need for balancing the corrosion rate and mechanical properties of the material [9]. Therefore, Fe-based alloys represent

a special class of materials: mechanical stability is desired yet the corrosion rate needs to be artificially increased using alloying, changing microstructure, porosity, surface treatments or galvanic coupling. The problem with the latter strategy is the potential intensification of cathodic oxygen reduction, acid-base separation, and corrosion-product precipitation in the layer immediately adjacent to the implant.

Another issue with in vitro characterization is the strong dependence of the results on the test medium. The presence of chloride enhances dissolution, bicarbonate and phosphate buffer the system and participate in precipitation, calcium changes the surface chemistry. Several critical reviews on bioabsorbable metals testing show how important the medium choice is for the measurement results [10]. Material characterizations of Fe-based alloys in Hanks' Balanced Salt Solutions also show how electrolyte composition changes degradation and corrosion product formation [11]. Measurements of pH and dissolved oxygen concentration show that different media also affect the local reaction field [12]. Tests performed without calcium tend to exaggerate open dissolution, tests performed with calcium may temporarily inhibit reactions through Ca-P coverage. None of those strategies is correct as such, both reveal different aspects of the degradation path. The problem is that a material to be used in contact with tissue needs to function in an environment where ions, flow, proteins, cells and corrosion products continuously interact. That is why modern bioabsorbable-metal tests tend to focus more on the mechanistic interpretation of the medium chemistry than on just the comparison of the corrosion rates in a single medium.

Manganese has been one of the key alloying elements in biodegradable Fe alloys. Fe-Mn alloys have been researched as degradable stent materials as Mn alters phase composition, magnetic response, corrosion and cytotoxicity of such materials [13]. Also, the research showed that Mn content can be used to tailor Fe-based alloys for biomedical applications [14]. Microstructure, mechanics, corrosion and cytotoxicity of hot-forged FeMn30 have also been characterized [15]. FeMnC(Pd) alloys have demonstrated that noble phases can modify degradation performance [16]. Powder-metallurgical Fe alloys with Pd, Ag and C content have provided further evidence that minor alloying changes both microstructure and corrosion of the alloy [17]. The effect of Mn is not only in accelerating the corrosion of Fe, yet depends on Mn content, powder processing, thermomechanical treatment, porosity, flow, chloride and ability of the degradation products to adhere or penetrate. Fe35Mn stent studies have shown that Mn content influences the degradation behavior of the implants [18]. Sintered Fe-based metallic foams have demonstrated that porosity is crucial for biodegradable Fe-based bone substitutes [19]. Porous Fe-based scaffold research further confirms that Mn is connected to microstructure, mechanical properties, biodegradability and biocompatibility [20]. The corrosion of Fe-30Mn-1C in chloride-containing solutions has shown strong environmental influence on the measured results [21]. Such ambiguity highlights the necessity of local measurements because bulk mass loss or a single electrochemical current cannot capture the anodic-cathodic separation.

Powder metallurgy emphasizes the importance of local measurements as the fabrication process creates a chemically and geometrically heterogeneous surface even before immersion. Particles' boundaries, residual porosity, oxide films and incomplete homogenization can all become preferred pathways for solution ingress and localized dissolution. In Fe-Mn-Ag alloys, this heterogeneity is not only a defect population, but the intended corrosion architecture. Ag-rich particles need to be electrically accessible enough to promote Fe-Mn corrosion, yet too great accessibility can lead to excessive cathodic oxygen reduction. Such porosity, increasing the surface area, can either help gradual degradation or form small domains with disproportionately high oxygen demand. This is why a local measurement method is preferable to a single bulk electrolyte value in the present work.

Addition of silver is an even more direct method of promoting Fe-Mn degradation. The noble Ag-rich particles act as local cathodes that drive micro-galvanic corrosion around them. Mechanically alloyed Fe-Mn-Ag material has been proposed as a way to combine accelerated degradation and antibacterial properties [22]. Also, selectivelaser-melted FeMn-Ag alloys show how Ag-rich regions influence the corrosion of Fe-based implants [23]. Nano- and bimodal structured Fe-Mn-Ag alloys have further confirmed the accelerated corrosion of Fe-Mn due to microstructure and galvanic effects [24]. Silver ion implantation into pure Fe has been researched as a means to modify the degradation and biological response of the alloy [25]. The advantage of the above method is obvious: a noble phase provides additional driving force for Fe-Mn dissolution without destabilizing the whole alloy. Yet the danger is equally obvious: cathodic stimulation is mostly expressed via oxygen reduction in physiological media. A material that is capable of fast degradation thanks to Ag-rich cathodes will also have an increased local demand for dissolved oxygen. This is especially important for the tissues that are directly exposed to Fe-based implant and where oxygen availability influences cell metabolism, inflammation and corrosion product evolution.

The electrochemical coupling can be summarized by the reactions that occur close to the surface. Oxygen reduction consumes dissolved oxygen and generates hydroxyl ions,

$$O_2 + 2H_2O + 4e^- \rightarrow 4OH^-, \tag{1}$$

whereas Fe dissolution supplies soluble metal ions,

$$Fe \rightarrow Fe^{2+} + 2e^-. \tag{2}$$

Those ions then hydrolyse and can lower local pH,

$$Fe^{2+} + 2H_2O \rightarrow Fe(OH)_2 + 2H^+, \quad (3)$$

while ferrous hydroxide may undergo further oxidation,

$$4Fe(OH)_2 + O_2 + 2H_2O \rightarrow 4Fe(OH)_3. \quad (4)$$

Thus, these examples illustrate the reasons why the two parameters, i.e., pH and oxygen content, cannot serve as interchangeable criteria of corrosion intensity. The process of oxygen reduction can result in an increase of pH level at the cathodic spots, hydrolysis can decrease pH levels in proximity to the dissolving metal, and precipitation can deprive the solution of excess hydroxyl ions prior to recording significant pH changes.

The specific composition of the simulated physiological solution plays a crucial role in such relationship between oxygen content and pH. Hanks' Balanced Salt Solution includes the chloride, bicarbonate, phosphate, and glucose. The calcium-containing Hanks' Balanced Salt Solution contains additional calcium and magnesium ions. Calcium and phosphate can precipitate close to the alkaline cathodic domains and form calcium-phosphate compounds, which are able to temporarily prevent the oxygen penetration. Reviews on bioabsorbable metals corrosion testing reveal that medium choice can affect degradation rate and products chemistry [10]. The direct analysis of corrosion of Fe-based alloys in Hanks' Balanced Salt Solutions proves that calcium-containing and calcium-free media can result in formation of different surface products and corrosion behavior [11]. In case of Fe-Mn-Ag alloys, such factor becomes crucial due to the fact that the calcium-phosphate compounds can inhibit the oxygen reduction in the early stages of immersion and then become porous, detachable or undergo chemical transformations.

Quasi-simultaneous local pH and dissolved oxygen measurements provide the direct access to the interface. Methods of simultaneous local mapping prove that the local current density, pH, and dissolved oxygen concentration can be recorded simultaneously in proximity to the electrochemical surface [26]. Localization of the electrochemical techniques confirms the importance of spatially-resolved analysis of corrosion and inhibition processes [27]. Non-invasive protocols of optical microsensors can be applied to measure local oxygen concentration [28]. The electrochemical investigations of the local pH help to understand why interfacial values can differ considerably from bulk values [29]. The local pH measurements near the surfaces of Mg alloys in simulated body fluids also reveal the dynamic evolution of local pH during the biodegradation process [30]. For Fe-Mn-Ag alloy series, pH and oxygen were measured at the distance of 50 μm from the degrading surface immersed into the flowing HBSS or HBSS+Ca. Such height was chosen to be able to monitor the localized reaction field but being far enough not to interfere with direct probe contacts with the corrosion products. Thus, the main question is whether the local pH value alone can be used as the criteria of the most extreme interfacial condition, or the buffered oxygen loss leads to another ranking of alloy-electrolyte combinations.

2. Materials and analytical method

The material series included commercially pure Fe, Fe35Mn, and (Fe35Mn)5Ag. Fe35Mn alloy was considered as the modified by Mn Fe alloy, and (Fe35Mn)5Ag was referred to as Ag-containing galvanic alloy. The powder processing technique used Fe powder with particle size below 45 μm and 99% purity, Mn powder with particle size below 10 μm and 99.6% purity, and Ag powder with particle size of 4–7 μm and 99.9% purity. The powders were mixed for 5 hours using stainless steel balls, uniaxially pressed, sintered, machined, mounted, and polished before the tests. The local pH and dissolved oxygen investigation presents the interfacial behavior of such material series [12]. The companion material characterization study provides the details on alloy preparation and corrosion test procedure [11]. In case of Ag-containing alloy, the Fe/Mn ratio was kept equal to 65/35 while adding 5 wt.% Ag. The mentioned microstructural features of the materials under consideration are crucial since Fe represents the simplest galvanically complex surface, Fe35Mn represents the Mn-rich heterogeneity and MnO regions, and (Fe35Mn)5Ag contains Ag-rich cathodic sites in the Fe–Mn alloy body.

The physical structure in Figure 1 connects the alloy composition with the surfaces which will later interact with HBSS and HBSS+Ca. It is evident from the three-column layout that this comparison is not confined to composition since the same sequence of powder metallurgy results in the formation of different reaction surfaces in the case of Fe, Fe-Mn doped with Mn, and Fe-Mn containing Ag. This latter alloy is particularly relevant due to the presence of noble particle cathodes in a more reactive Fe-Mn matrix.

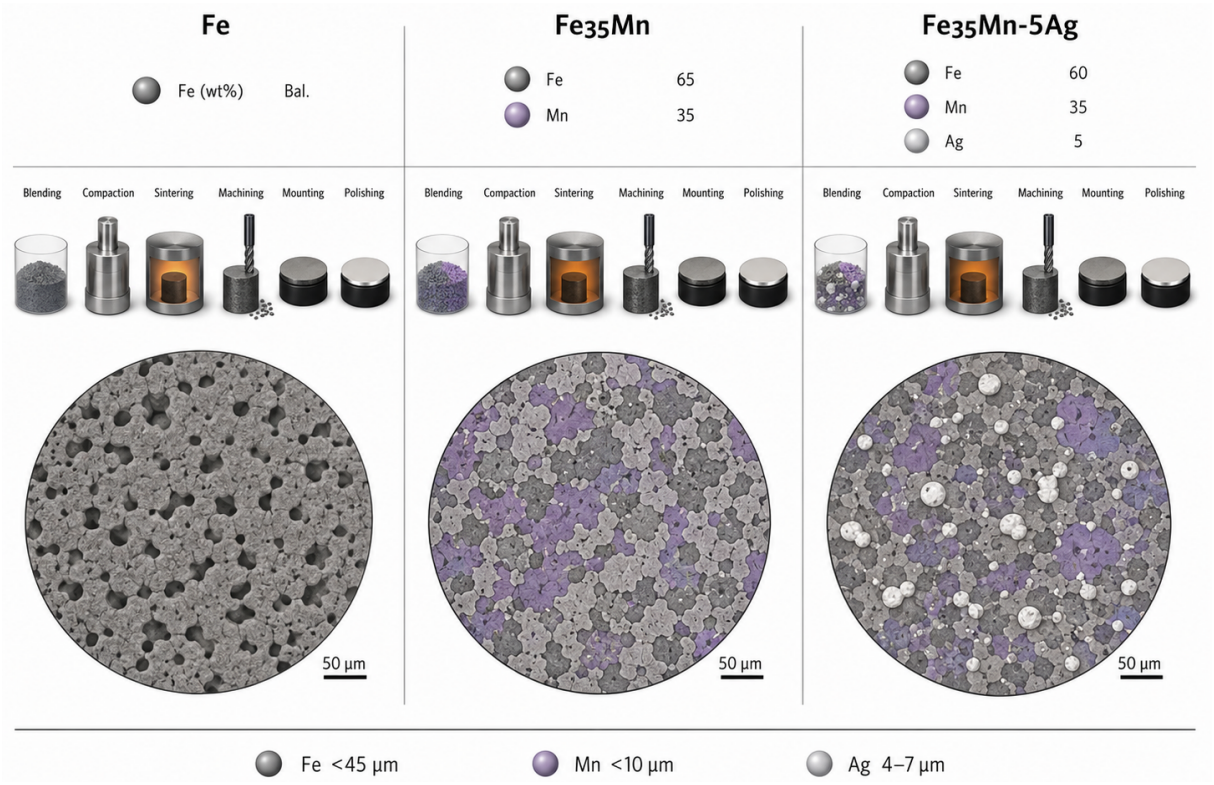

Figure 1: Alloys and processing route.

The geometry of the probes illustrated in Figure 2 determines the scale at which the interpretation of the results occurs in terms of the near-interface solution, and not the bulk electrolyte. The pH microelectrode had a 10 μm tip diameter and 50 μm tip length, while the oxygen micro-optode made use of a 50 μm needle-type tip. Both of the sensors were located 50 μm above the surface of the alloy and the lateral distance between the tips of the probes was also 50 μm. All measurements were performed at 37 °C with a 1.0 $mL.min^{-1}$ hydrodynamic flow rate. The initial mapping was done on 4000 μm × 4000 μm with 200 μm spacing, and then higher resolution scanning was performed on 2000 μm × 4000 μm with 80 μm spacing, thus producing measurement grid of size 25 × 50. The rapid (Fe35Mn)5Ag measurements in HBSS were done using line scans with 50 μm spacing and a 5 s sampling time [12].

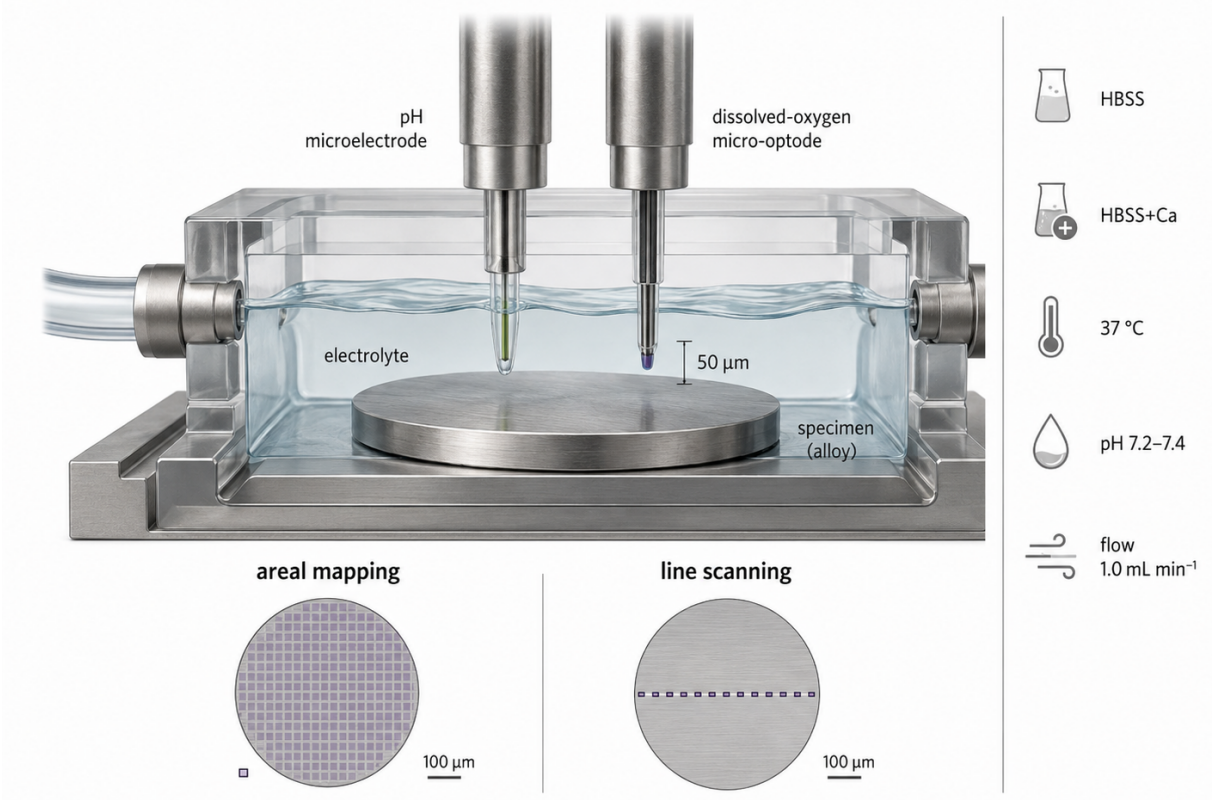

Figure 2: Flow cell and probe placement.

There are two electrolytes which are significant for the comparison. The calcium-free HBSS was made up of 5.333 mM KCl, 0.441 mM KH_2PO_4, 4.167 mM $NaHCO_3$, 137.9 mM NaCl, 0.338 mM Na_2HPO_4, and 5.556 mM D-glucose. While in HBSS+Ca, apart from using the same base solution, the other ingredients used were 1.261 mM $CaCl_2$, 0.493 mM $MgCl_2.6H_2O$, and 0.407 mM $MgSO_4.7H_2O$. Both media had an initial pH of 7.2–7.4. The material characterization study describes the roles played by these media in corrosion and products formation [11]. Local interfacial analysis explains how this compositional change impacts pH and dissolved oxygen concentration at the metal surface [12]. This compositional change brings in a precipitation pathway which is not present or weak in calcium-free HBSS. In HBSS, there is a possibility of the formation of iron and manganese phosphates but not very protective. On the other hand, in HBSS+Ca, rapid deposition of Ca–P containing phases can take place in locally alkaline sites.

Table 1: Measurement basis.

Category	Specific basis used in the analysis
Alloys	Commercially pure Fe, Fe35Mn, and (Fe35Mn)5Ag; Fe:Mn ratio preserved at 65:35 in the Ag-containing composition.
Powders	Fe $< 45\,\mu$m and 99% purity; Mn $< 10\,\mu$m and 99.6% purity; Ag 4–7 μm and 99.9% purity.
Processing	Powder mixing for 5 h, uniaxial compaction, sintering, machining, resin mounting, and final polishing.
Exposure	HBSS and HBSS+Ca at initial pH 7.2–7.4, 37 °C, and 1.0 $mL.min^{-1}$ flow.
Local measurements	pH and dissolved oxygen recorded 50 μm above the alloy surface by microelectrode and micro-optode probes.

The information in Table 1 establishes the point of comparison relative to the alloy-electrolyte measurements. Distinctions between the three different alloys cannot be boiled down to a single iron response since the surface chemistry will have been changed by manganese-enriched heterogeneous spots and silver-enriched cathode spots. Similarly, distinctions between HBSS and HBSS+Ca cannot be attributed to minor variations in ionic strength, since the calcium and phosphate ions provide a way for the products to form in cathodically basic regions. The important result is thus the joint variation of pH and O_2 over the surfaces.

Three parameters are used to quantify differences between the measurement intervals. The obvious pH difference is expressed as

$$\Delta\mathrm{pH} = \mathrm{pH}_{\max} - \mathrm{pH}_{\min}. \tag{5}$$

The normalized oxygen loss is written as

$$L_{\mathrm{O_2}} = \frac{C_{\mathrm{air}} - C_{\min}}{C_{\mathrm{air}}}, \tag{6}$$

where $C_{\min}$ is the minimum measured dissolved oxygen concentration and C_{air} is taken as 5.8 $mg.L^{-1}$, the approximate aerated oxygen level for HBSS near 37 °C. The oxygen–pH discordance ratio is defined as

$$\Psi = \frac{L_{\mathrm{O_2}}}{\Delta\mathrm{pH} + 0.05}. \tag{7}$$

This ratio is not a material constant, but rather an indicative value for the current alloy and electrolyte combination, when a large number means a relatively large degree of oxygen exhaustion compared to the visible span of pH variation. A small constant in the denominator avoids the artificial divergence when the pH interval is small.

The correlated descriptors distinguish clearly the aggressively acting interface and the hidden one. Openly aggressive interface is characterized by a high value of oxygen depletion and pH window. The hidden oxygen sink shows a high oxygen depletion but a small pH interval due to the neutralization of the hydroxyl ions produced by oxygen reduction at the Ca–P precipitation or at corrosion product transformation. Thus, the descriptor Ψ is most relevant for the situations, when pH and oxygen differ. It reveals the condition, when an interface is close to neutrality but actively acting.

3. Results and discussion

The first calcium-free HBSS exposure gave the most convincing results regarding the Ag-induced micro-galvanic reactions. For pure Fe pH varied from 6.76 to 7.36, while oxygen concentration changed from 2.40 to 4.10 $mg.L^{-1}$. Fe35Mn showed the narrowest pH window, between 7.20 and 7.39, with the oxygen range of 2.00 to 3.90 $mg.L^{-1}$. In contrast, the sample containing Ag had a quite different behavior. Within the first 20–60 minutes of the exposure, (Fe35Mn)5Ag formed a pH window from 6.40 to 8.10, with the oxygen concentration from 0.50 to 1.40 $mg.L^{-1}$. This early result confirms that Ag-rich particles do not merely accelerate Fe–Mn-phase dissolution; they create intense local cathodic demand for oxygen.

Table 2: Initial HBSS windows.

Alloy	pH min.	pH max.	ΔpH	DO min. ($mg.L^{-1}$)	L_{O_2}	Ψ
Fe	6.76	7.36	0.60	2.40	0.586	0.90
Fe35Mn	7.20	7.39	0.19	2.00	0.655	2.73
(Fe35Mn)5Ag	6.40	8.10	1.70	0.50	0.914	0.52

The descriptors in Table 2 differentiate between absolute oxygen severity and the masking effect of pH. (Fe35Mn)5Ag is the material with highest oxygen depletion, with the smallest Φ_{min} being equivalent to more than 90% reduction of the aerated oxygen reference. Its Ψ is smaller only due to the very large range of the pH descriptor. Therefore, the problem is not masked: the pH descriptor itself shows clearly that there are localized corrosion conditions due to the presence of acidic and alkaline spots. Fe35Mn has less extreme oxygen depletion, but a much smaller pH range, resulting in a larger discrepancy ratio. The example demonstrates that the ranking of materials by the pH range alone does not account for the oxygen descriptor of Fe35Mn, while the ranking of oxygen minimum values does not reveal the difference between visible and masked chemical polarization.

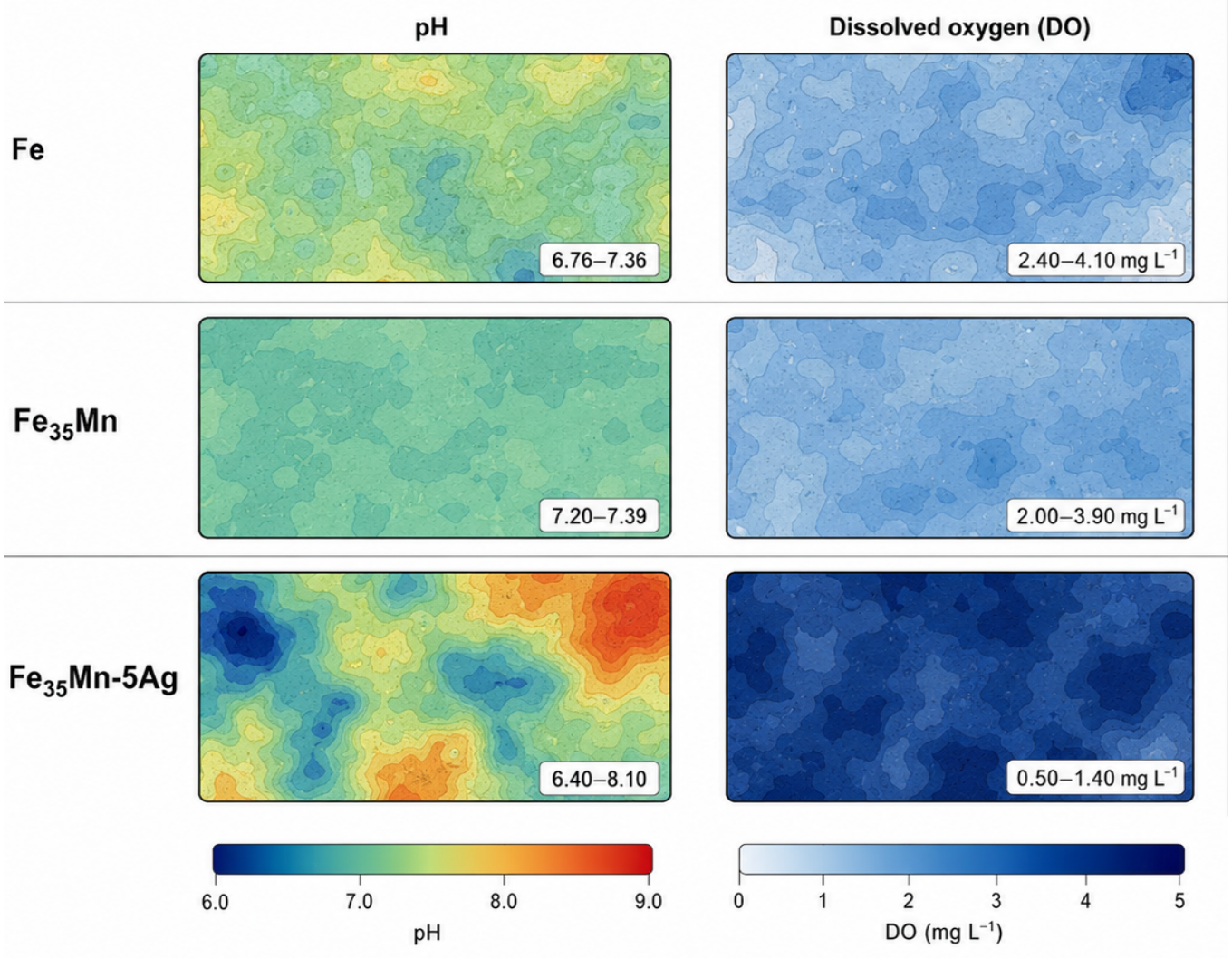

Figure 3: Initial HBSS fields.

Fe and Fe35Mn have yet another property for comparison. Whereas pure Fe had a larger initial pH range than Fe35Mn, implying greater local acid–base segregation, Fe35Mn had a lower oxygen minimum although it had a smaller pH range. Thus, the presence of Mn in heterogeneous form influences the hydrolysis and reduction balance and not just the total increase of the corrosion activity. This means one cannot regard Fe35Mn merely as a faster corroding alloy of Fe.

Maps shown in Fig. 3 provide evidence supporting the role of Ag-rich regions in the oxygen reduction process. Regions with acidic pH are associated with the dissolution of the Fe and Mn compounds and their hydrolysis, while regions with higher pH values are associated with cathodic oxygen reduction reaction. Proximity of these regions makes the (Fe35Mn)5Ag surface more chemically heterogeneous than Fe or Fe35Mn surfaces. In the context of implant evaluation, this is an important

fact because acidic and alkaline regions may coexist at the near surface boundary layer of the material. The bulk pH average value would smoothen these extremes, and actual chemical environment experienced by cells and proteins would be concealed.

Monitoring of the initial state of (Fe35Mn)5Ag in rapid HBSS experiments has revealed that the initial state was not a transient phenomenon occurring during early wetting. During the first several hours, the scans have shown clear acidity peaks near pH 6.7–6.9 and cathodic regions with higher pH values. Further product formation made the pH contrast weaker, but the level of dissolved oxygen still remained low, approximately 0.75-1.20 $mg.L^{-1}$. At 15 h, the amount of corrosion products formed became so significant that interfered with the probes operation and stopped the experiment to protect the microelectrode and micro-optode [12]. The important fact here is that the pH contrast became weaker but the oxygen level remained high.

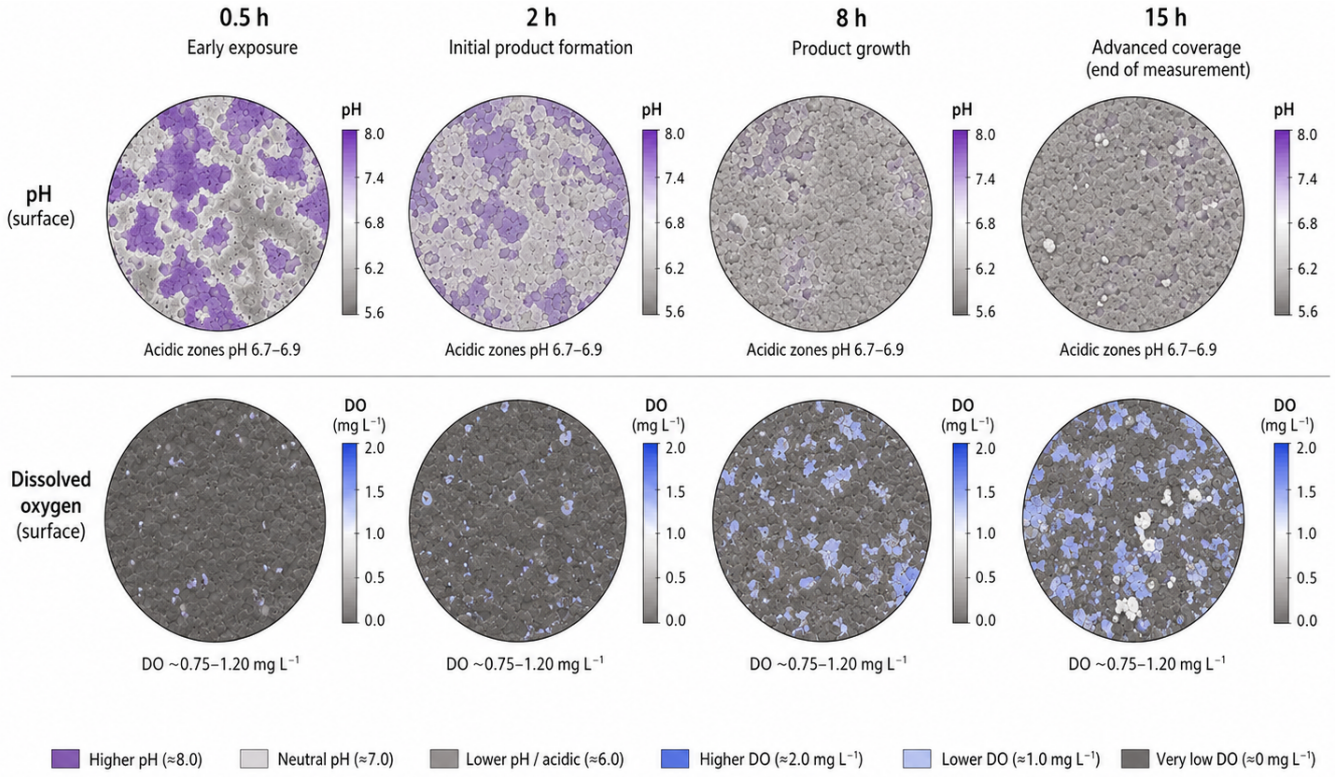

Figure 4: FeMnAg in HBSS.

The time sequence in Fig. 4 shifts the interpretation of corrosion products. Their formation is usually considered a process leading to passivation, but in the case of Fe–Mn–Ag, it results in the development of less stable conditions. The surface is covered with products, and the pH field becomes less pronounced, whereas oxygen depletion is still significant. Such behaviour may be explained by oxygen reduction on the Ag-enriched cathode and oxidation of ferrous compounds, resulting in oxygen consumption. Corrosion products act as an active layer, which modifies the transport rather than being a stable passive layer.

Pure Fe and Fe35Mn in calcium-free HBSS demonstrated a slow evolution. After 12 h of contact, Fe had pH of 7.07–7.22 and oxygen level of 1.90–3.00 $mg.L^{-1}$. In the next 24 h, the pH rose to 7.09–7.27, whereas oxygen became depleted to 1.55–2.05 $mg.L^{-1}$. Fe35Mn showed slightly higher values of pH (alkaline character) and lower values of acidity (pH was 7.23–7.28 and 7.20–7.32 for 12 and 24 h, respectively). Oxygen decreased from 2.38–2.60 $mg.L^{-1}$ to 1.78–2.26 $mg.L^{-1}$. These values indicate that the visible pH field narrowed for both alloys, but the oxygen concentration continued to fall.

Table 3: Late HBSS windows.

Alloy	Time	pH range	DO range ($mg.L^{-1}$)	L_{O_2} at DO min.	Ψ
Fe	12 h	7.07–7.22	1.90–3.00	0.672	3.36
Fe	24 h	7.09–7.27	1.55–2.05	0.733	3.19
Fe35Mn	12 h	7.23–7.28	2.38–2.60	0.590	5.90
Fe35Mn	24 h	7.20–7.32	1.78–2.26	0.693	4.08

As demonstrated in Table 3, the late HBSS values are an example of why near-neutral pH should not be considered

a safe endpoint for the analysis. Fe and Fe35Mn were still near neutral pH after 12–24 h, yet had significant oxygen loss normalization. The case of Fe35Mn is particularly illustrative. After 12 h, the pH span of Fe35Mn was just 0.05 pH units, while oxygen loss was 2.38 $mg.L^{-1}$. The large Ψ factor represents a case where pH buffering or averaging does not reveal continued oxygen depletion. While Mn compounds reduce the effects of acidification, they do not address oxygen consumption.

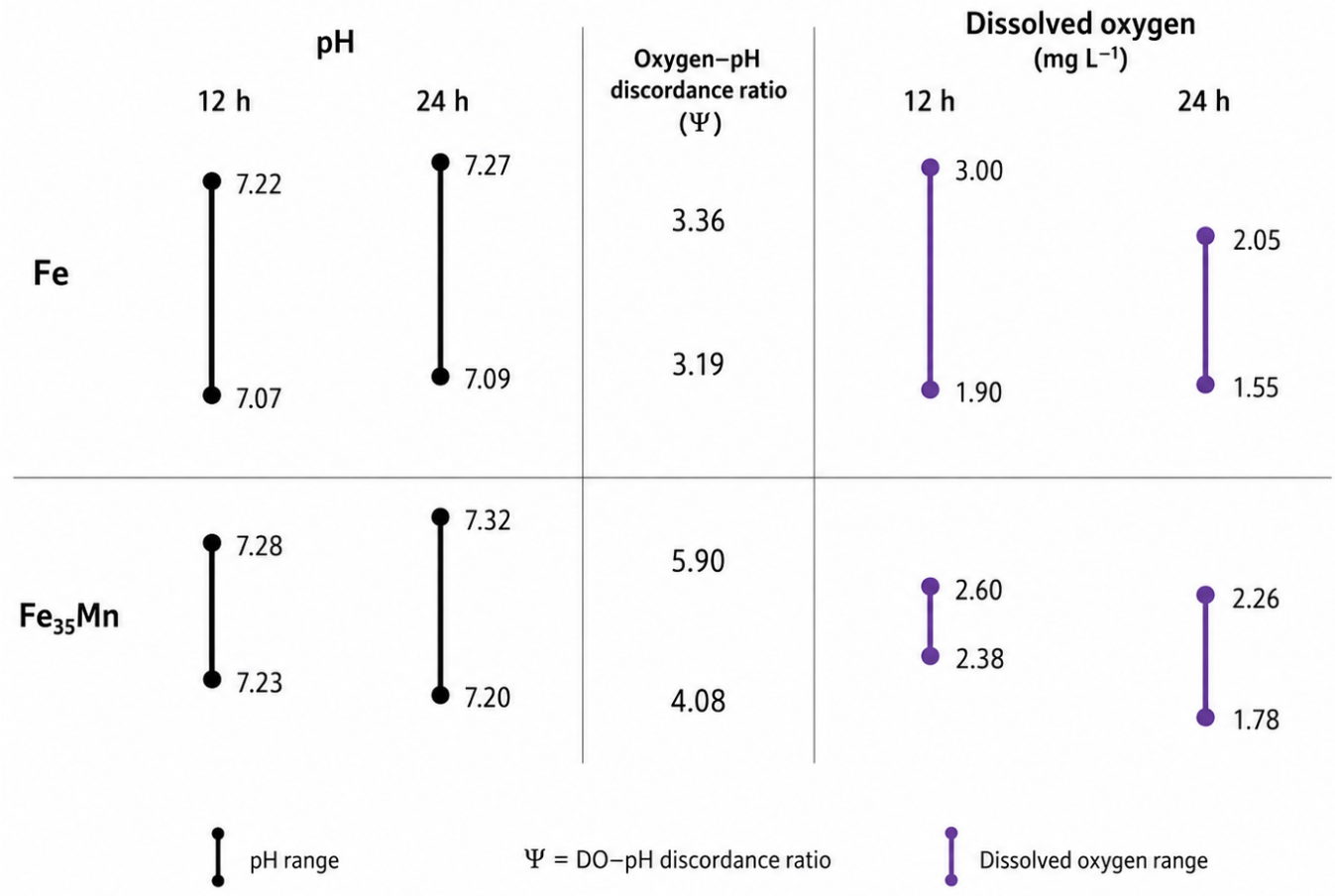

Figure 5: Late HBSS windows.

The second map shown in Figure 5 supports the above conclusion. Even though the Fe and Fe35Mn do not show the distinct pH contrast observed originally in the (Fe35Mn)5Ag, they exhibit consumption of oxygen in their respective maps. Hence, corrosion-product covering and pH neutralization cannot be taken as the signs of low reactivity. For biodegradable alloys of Fe, late stages require not only maintenance of mechanical integrity of the material, but maintenance of oxygen consumption by the product-covered surface. Tissue-facing environment can thus have stable pH, but still undergo oxygen depletion.

Addition of calcium modified the initial corrosion behavior most significantly in the case of Ag-containing alloy. The initial pH ranges of Fe, Fe35Mn, and (Fe35Mn)5Ag in HBSS+Ca were 7.05-7.30, 7.16-7.30, and 7.10-7.80 respectively. The initial oxygen behavior was more informative. The initial oxygen levels for Fe, Fe35Mn, and (Fe35Mn)5Ag were 1.20-4.40, 4.15-4.80, and 4.90-5.65 $mg.L^{-1}$ correspondingly. Compared with the 0.50–1.40 $mg.L^{-1}$ oxygen range for (Fe35Mn)5Ag in calcium-free HBSS, the calcium-containing solution initially suppressed oxygen depletion almost completely.

Table 4: Initial HBSS+Ca windows.

Alloy	pH min.	pH max.	ΔpH	DO min. ($mg.L^{-1}$)	L_{O_2}	Ψ
Fe	7.05	7.30	0.25	1.20	0.793	2.64
Fe35Mn	7.16	7.30	0.14	4.15	0.284	1.50
(Fe35Mn)5Ag	7.10	7.80	0.70	4.90	0.155	0.21

It is evident from the initial HBSS+Ca data in Table 4 that the influence of calcium was not uniform to all the alloys. It may be observed that the Ag-containing alloy, which is the most oxygen depleting alloy in calcium-free HBSS solution, becomes the least oxygen depleting alloy in the early calcium solution. This could be due to rapid formation of Ca-P containing products on the cathodically active areas. These products will result in consumption of hydroxyl ion, reduction

of pH gradient, and limited oxygen diffusion. Pure Fe, however, did not enjoy the same advantage, as shown by its minimum of 1.20 $mg.L^{-1}$ oxygen even in the early period of time. Calcium does not work simply to improve the buffering effect; its effectiveness will depend on the interactions between product nucleation, surface coverage, and oxygen exposure relative to the microstructure of the alloy.

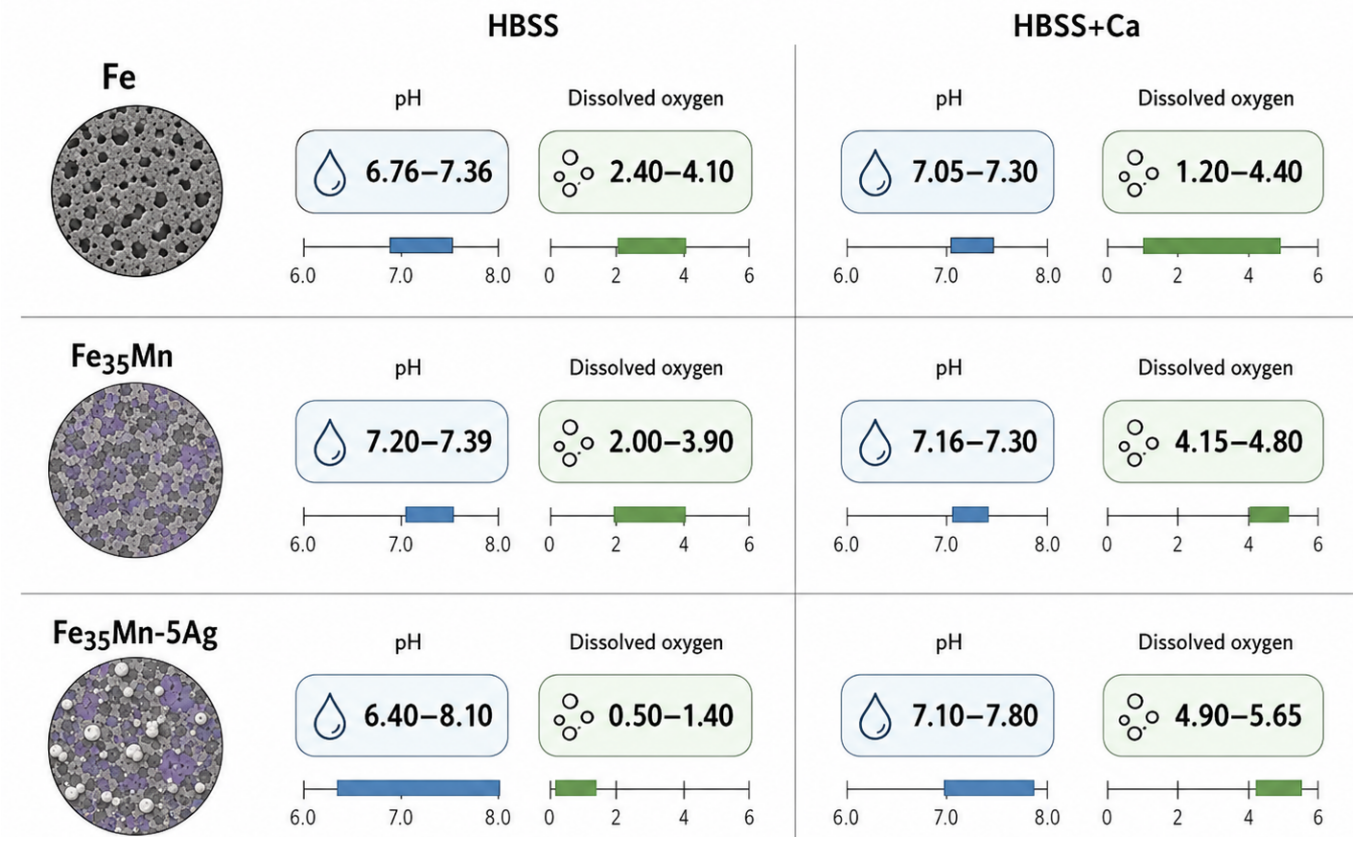

Figure 6: Early calcium effect.

It is evident from the comparison shown in Figure 6 that there is a transitory protective function of the Ca–P deposits. In contrast to the early (Fe35Mn)5Ag behavior, which is not mild since Ag is not the cathodic phase anymore, it is mild because oxygen access to cathodic sites is restricted. This has consequences for the design of coatings. Cathodic accelerators are well-controlled when in a calcium-containing environment as long as the initial deposit layer is intact and does not break or becomes permeable. The same substance turns into an aggressive one after the loss of integrity of that layer.

The 24 h (Fe35Mn)5Ag behavior in HBSS+Ca further supports the idea of transient protection. At 2 h, pH was 7.14-7.54 and oxygen content was 5.28-5.64 $mg.L^{-1}$. After 6 hours, pH values were slightly higher than 7.23-7.45 with 5.06-5.50 $mg.L^{-1}$ of oxygen. By 12 h, there was a dramatic fall in oxygen content to 2.50-5.20 $mg.L^{-1}$, while pH was 7.13-7.40 . However, at 24 hours, the oxygen concentration was 0.40–4.00 $mg.L^{-1}$, whereas pH varied from 7.16 to 7.31. This is the best example that proves decoupling between pH and oxygen.

Table 5: FeMnAg in HBSS+Ca.

Time	pH range	DO range ($mg.L^{-1}$)	ΔpH	L_{O_2}	Ψ
2 h	7.14–7.54	5.28–5.64	0.40	0.090	0.20
6 h	7.23–7.45	5.06–5.50	0.22	0.128	0.47
12 h	7.13–7.40	2.50–5.20	0.27	0.569	1.78
24 h	7.16–7.31	0.40–4.00	0.15	0.931	4.66

The trend presented in Table 5 serves as the basis for the oxygen masking effect. While the oxygen/pH disparity ratio was equal to 0.20 after 2 h, it reached 4.66 after 24 h. This substantial change did not happen due to pH reaching more extreme values, but rather happened as the oxygen depletion process strengthened with pH being squeezed. Such behavior indicates the formation of the Ca-P containing coating which was initially able to hinder the oxygen diffusion, but then lost its property of acting as a barrier by detaching, cracking, becoming porous, or changing its structure chemically. Thus, the oxygen reduction could continue when oxygen reached the Ag rich cathodic regions again.

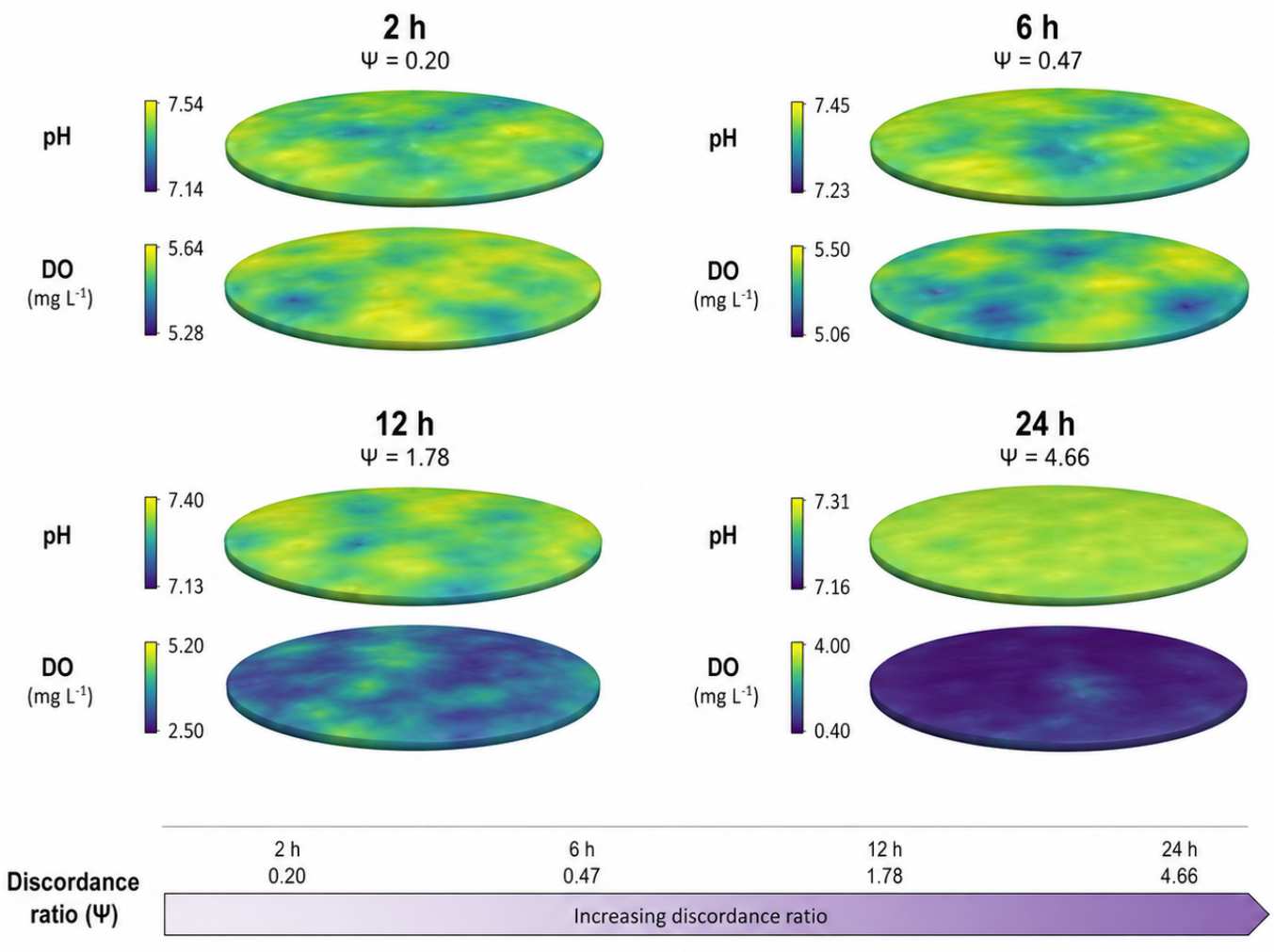

Figure 7: FeMnAg in HBSS+Ca.

The temporal maps in Figure 7 reveal the mechanism of pH masking. The initial stage shows signs consistent with the presence of an interface coated with Ca–P deposits, but the later stages display oxygen deficiency without any concomitant increase in the size of the alkaline area, which indicates active pH neutralization reactions and not the lack of corrosivity. In the case of Fe–Mn–Ag biodegradable implants, pH neutrality maintained via chemical reactions acquires particular importance due to the presence of calcium and phosphate in tissue-facing fluids. Thus, a material can pass the initial pH test and develop an oxygen-depleting surface after the changes in product layer.

The late-stage response of FeMnAg explains why the addition of calcium into the immersion medium should not be regarded solely as a protecting effect. Calcium and phosphate reduce early activity of cathodic regions due to the formation of deposits in locations of hydroxyl ion generation. However, such deposits are still an integral part of a dynamic corrosion system and can allow re-opening of oxygen paths and further oxygen reduction in the sites which were initially cathodic. As a result, a deceiving surface is formed: the solution in contact with the alloy demonstrates acceptable pH according to physiological criteria, while the level of oxygen can be extremely low. This numerical transformation from high oxygen levels at 2–6 h to low oxygen levels at 24 h is more informative than any of the endpoints separately.

Cases of pure Fe and Fe35Mn in HBSS+Ca are different. Pure Fe got covered with bright products rapidly, and the extent of coverage increased with time. Its minimum pH rose from 7.03 at 1 h to 7.22 at 24 h, while oxygen concentration reduced to approximately $0.45\,mg.L^{-1}$. The coverage of the material with products did not stop oxygen access and/or their consumption. Fe35Mn kept the minimum pH near 7.10 during 24 h, and the pH maximum increased slightly from 7.23 to 7.32. Its oxygen minimum was reduced from 3.15 to $1.90\,mg.L^{-1}$, and the oxygen interval at 24 h was 1.90–$4.30\,mg.L^{-1}$, wider and less oxygen-deficient than 1.78–$2.26\,mg.L^{-1}$ for Fe35Mn in HBSS without Ca.

In addition, from Figures 8(Fe) and 8(Fe35Mn), it becomes apparent that calcium-based products are more effective in moderating the oxygen consumption of Fe35Mn compared to Fe. In this case, the role of Mn could be associated with its impact on the properties of the product-covered surface, which decreases the intensity of the acidification process and reduces the oxygen depletion of the surface relative to pure iron. Therefore, the effect of Mn cannot be considered as an increase in the rate of corrosion, but just a weakening of polarization and oxygen depletion of Fe compared to (Fe35Mn)5AgT̈he effect can be called interfacial moderation of the reaction.

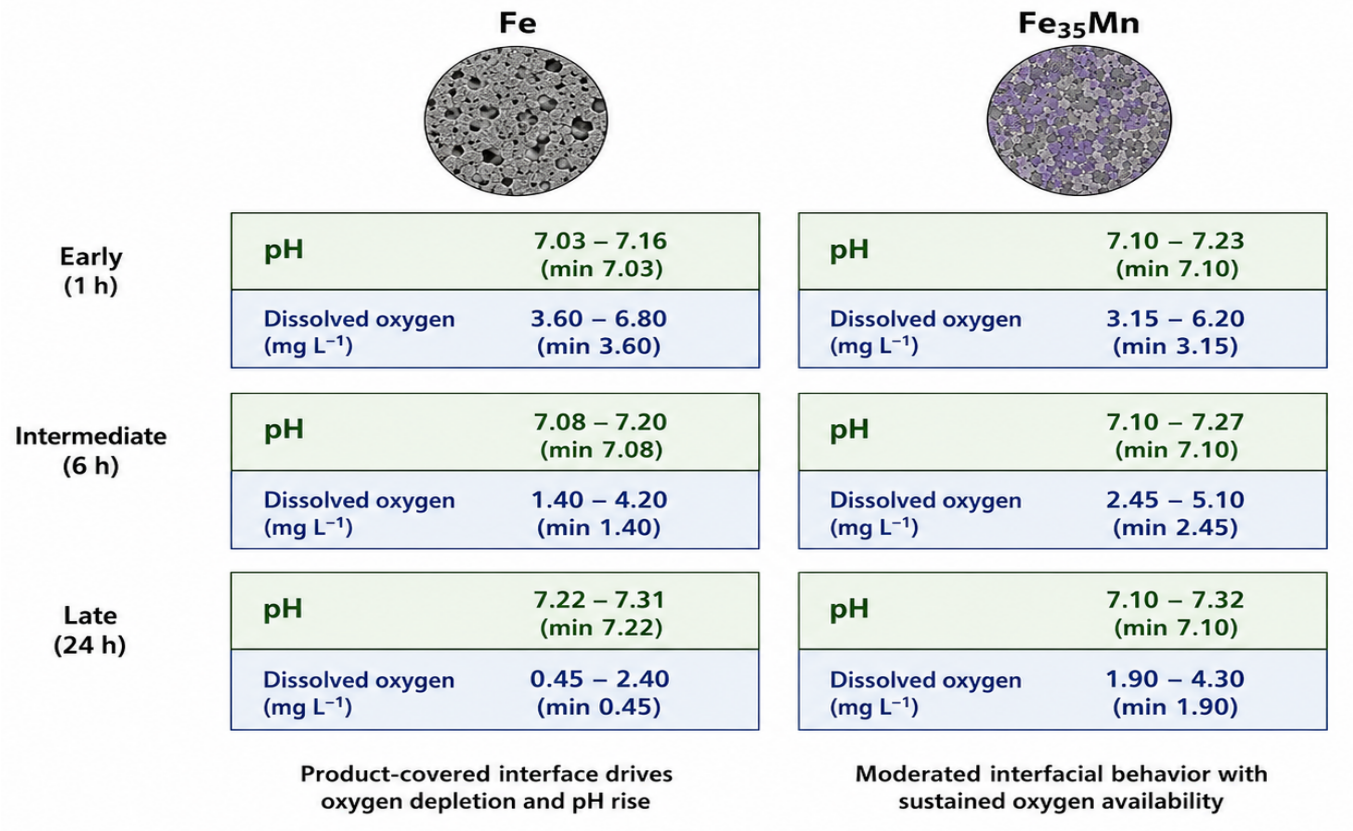

Figure 8: Fe and Fe35Mn in HBSS+Ca.

The state map in Figure 9 represents the response of the system in one-dimensional pH and oxygen space. In this case, the openly polarized area includes conditions with a significant oxygen depletion and large pH range, while the buffered-demand area includes conditions with small pH range and significant oxygen depletion. From this representation, it is evident why the late (Fe35Mn)5Ag response in HBSS+Ca is not chemically mild despite its close to neutral pH. It means that the material enters the region of high oxygen demand relative to the change in pH.

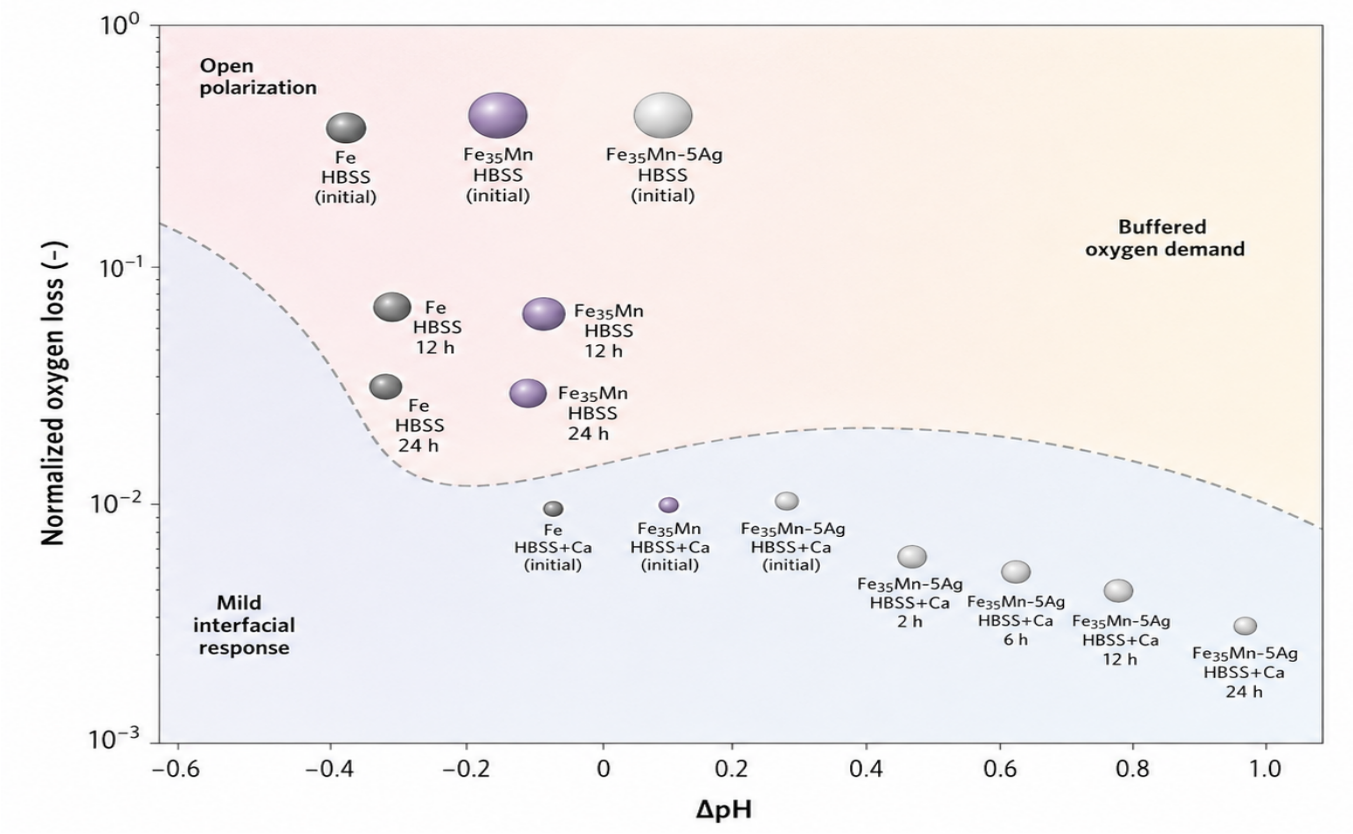

Figure 9: Interfacial state map.

Based on all of the above evidence, Ag in Fe–Mn alloys should be re-evaluated. In calcium-free HBSS, Ag forms an overtly aggressive micro-galvanic system characterized by strong oxygen depletion and wide pH differentiation. In HBSS+Ca, Ag shows initial controllability due to calcium-phosphate precipitation limiting oxygen availability; the final state, however, is more worrying due to oxygen depletion with a neutral pH. In other words, the same noble element creates two different risks for the biodegradation process. The first one can be seen in terms of pH and oxygen; the second one – only in terms of oxygen. This is why it is critical to measure local dissolved oxygen during the assessment of Fe–Mn–Ag biodegradable alloys.

The pathway described in Figure 10 summarizes the hierarchy that is evident in the results of paired measurements. Pure iron dissolves slowly and is able to deplete oxygen in the presence of product coverage. Fe35Mn alters the chemistry of products and tends to narrow the pH zone; nevertheless, it is not able to stop oxygen depletion. (Fe35Mn)5Ag accelerates the corrosion via cathodic sites enriched with Ag and results in the most intensive oxygen depletion, especially in calcium-free HBSS and at the late stage in HBSS+Ca. In case of calcium-containing solution, there is an extra product-gating effect. It may decrease oxygen availability in the beginning and then become weaker with time. The key parameter of the material in question is not maximum corrosion rate. It is the ability to undergo the controlled dissolution without the depletion of oxygen zone nearby the alloy.

The interpretation of the oxygen measurements requires care but does not imply ignoring the signal. The current set of measurements does not recreate vascular perfusion or cellular oxygen consumption and cannot be considered a direct indicator of tissue hypoxia. At the same time, they confirm the fact that the corroding alloy can act as an additional oxygen sink in the layer adjacent to the surface. In the case of temporary implants, this local oxygen demand might be linked to inflammation, protein adsorption, mineral deposition, and tissue ingrowth. Hence, the material accelerating corrosion via cathodic oxygen reduction will be shifting its corrosion load to the surrounding biological environment. The optimal design direction is not maximum galvanic acceleration but limited contrast resulting in the predictable dissolution process without permanent local oxygen depletion.

It also explains why some of the traditional test outputs might mislead the researcher. The bulk pH measurement provides information about the solution average value and does not distinguish between acid-producing dissolution and alkaline oxygen reduction. The surface producing both may seem to have a nearly neutral pH in the beaker. Impedance spectroscopy can indicate the presence of product layer but cannot prove the availability of oxygen nearby. The mass loss can measure the total degradation process but not tell what was the mechanism behind it. The pair of pH and oxygen measurements overcomes these issues by linking reaction chemistry and local exposure to the material surface. It does not substitute any other mechanical tests or biological evaluations; it only supplements them with an important interfacial criterion.

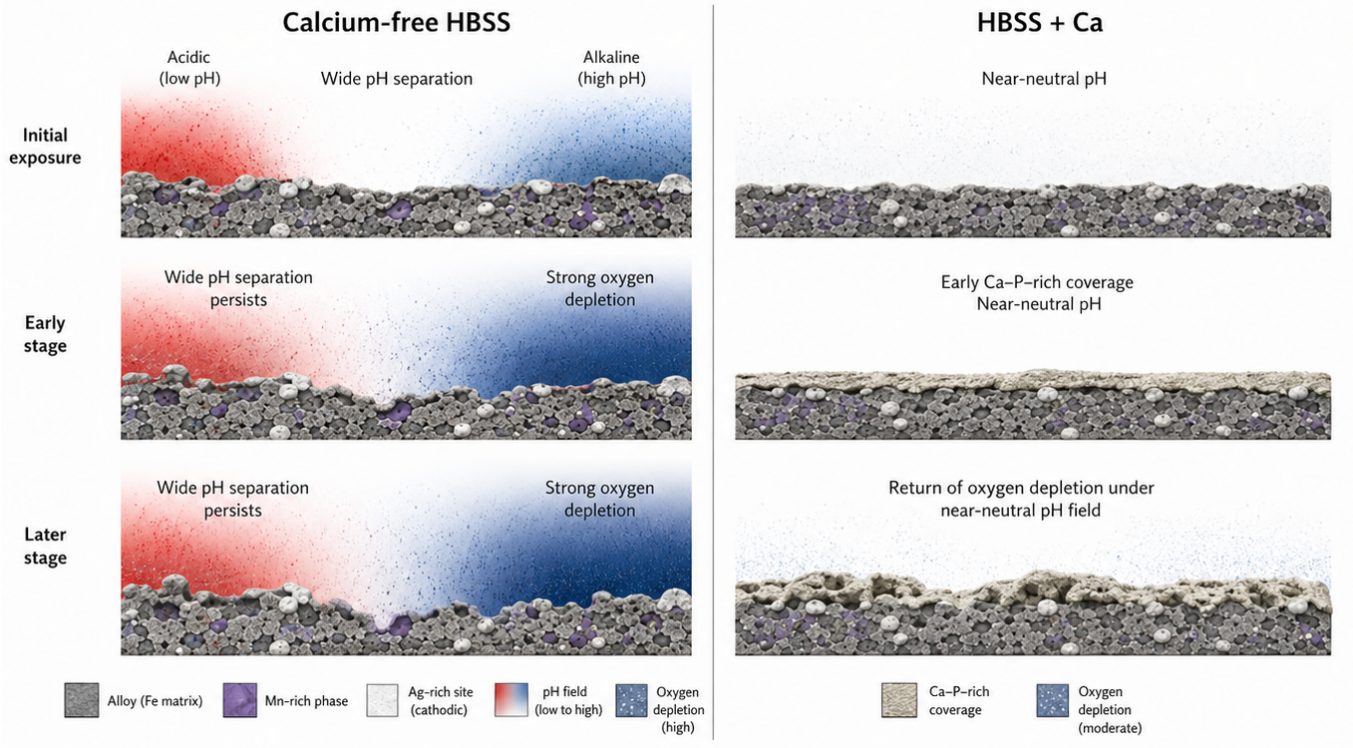

Figure 10: Mechanistic corrosion pathway.

These results also have implications for planning future experimentation. Early short exposures are valuable for identifying

fast galvanic activation, but they can overestimate the role of Ca–P coating in stabilization of the surface. Late tests are necessary to find out whether the first-formed product layer remains intact, becomes porous, or is detached. On the contrary, long-term immersion without early surface mapping can ignore the fast but dramatic acid-base dissociation that takes place when the Ag-rich cathodes start functioning. The combination of early and late pH–oxygen mapping, surface-product investigation, and assessment of the continuity of the product layer would provide the connection between alloy composition factors and both degradation speed and interfacial oxygen demand.

For the implant development, the conclusion is clear. For designing of Fe–Mn–Ag biodegradable implants, it is important to use the moderated cathodic alloy architecture. Such alloy should contain Ag-rich sites in such a way to increase dissolution rate, but not to accumulate oxygen reduction in stable cathodic sinks. Factors that control powder processing and Ag-particle size, pore connectivity, oxide content in particle boundaries, and product formation in post-sintering processes are not only metallurgical, but also oxygen-transport parameters. This also holds true for electrolyte-facing corrosion products. A good product layer should not occlude the surface, detach in large pieces, or transform with intense oxygen demand. The desirable state is the surface that corrodes moderately in distributed reactions, but not in isolated high-demand sites.

The data interpretation has a restricted scope. The pH span, oxygen loss, and oxygen–pH discordance ratio are calculated on the basis of the measured pH and dissolved oxygen windows, but not of a three-dimensional reaction-transport simulation. The measurement height of 50 μm is suitable for near-surface analysis, but it does not provide the oxygen concentration directly at the metal surface or in tissue. Measurement period covers from early to 24 hours behavior, except (Fe35Mn)5Ag in HBSS, for which line scan ended at 15 h due to excessive product layer formation. These parameters describe the interfacial corrosion for the selected alloys and electrolytes, but for translation of the oxygen-masking effect into biological performance, longer immersion, media with proteins, cell cultures, and dynamic tissue model should be used.

However, despite all restrictions, the data are conclusive enough to give an answer to the research question. Local pH alone is not enough to detect the most severe interfacial condition in Fe–Mn–Ag biodegradable alloys. In calcium-free HBSS, pH and oxygen identify aggressive (Fe35Mn)5Ag corrosion. In calcium-containing HBSS, (Fe35Mn)5Ag late surface deceives by narrow near-neutral pH window and low 0.40 $mg.L^{-1}$ oxygen concentration. This decoupling is not accidental; it reflects the mechanism of cathodic sites, oxygen reduction, Fe–Mn products oxidation, and Ca–P precipitation. The alloy screening without taking this decoupling into account may choose biodegradable alloys which are chemically moderate, but create oxygen-depleted interface.

The statement of the research result can be expressed in terms of division of interface control mechanisms by alloy series. Pure Fe is limited by the slowest degradation but still able to remove oxygen in case of reactive products. Fe35Mn changes the acid-base nature of corrosion but does not oxygenize the interface. (Fe35Mn)5Ag provides the clearest corrosion acceleration due to increased oxygen reduction in Ag-rich cathodes, but this acceleration strongly depends on the ability of electrolyte to maintain contact with these cathodes. Calcium-containing HBSS temporarily switches (Fe35Mn)5Ag from openly aggressive to covered mode, but 24 h measurement demonstrates that this covered mode can switch into oxygen-masked mode. The message is that alloy microstructure and solution chemistry play equal roles in the control of biodegradation of Fe-alloys.

The numerical comparison also reveals the indicator-dependence of ranking. By pH span, initially calcium-free (Fe35Mn)5Ag is the dominant event. By oxygen loss, 24 h (Fe35Mn)5Ag in HBSS+Ca becomes equally important despite its narrow pH window. By oxygen–pH discordance ratio, Fe35Mn in late HBSS exposure and (Fe35Mn)5Ag in 24 h in HBSS+Ca become important events due to disproportionate oxygen demand to pH changes. This indicator dependence supports the conclusion that the corrosion at biodegradable Fe-alloy interfaces is multi-reaction and transport-controlled.

4. Conclusions

The pH–oxygen measurements have shown that the corrosion chemistry of powder-processed Fe, Fe35Mn, and (Fe35Mn)5Ag in HBSS cannot be understood from pH alone. The research question was whether near-neutral pH is sufficient indicator of safe interfacial conditions, or the oxygen measurements will uncover additional corrosion demand. The answer is that near-neutral pH alone is not enough. In calcium-free HBSS, (Fe35Mn)5Ag generates openly aggressive micro-galvanic response with pH from 6.40 to 8.10 and dissolved oxygen decrease to 0.50 $mg.L^{-1}$ in the first hour. This condition is severe, but it is visible by both pH and oxygen changes.

Calcium-containing HBSS creates the more important diagnostic problem. Ca–P containing products initially protect (Fe35Mn)5Ag from corrosion by oxygen maintenance at the aerated level, but after 24 h, the minimum of oxygen concentration drops to 0.40 $mg.L^{-1}$ while pH remains between 7.16 and 7.31. Oxygen–pH discordance ratio increases from 0.20 at 2 h to 4.66 at 24 h. It confirms that the late (Fe35Mn)5Ag surface consumes oxygen intensively without broad pH change. Pure Fe also has product-covered oxygen depletion, while Fe35Mn moderates pH variation and partially reduces oxygen loss, but does not remove oxygen consumption.

The conclusion is that the Ag addition should be considered as oxygen-design problem, rather than just as degradation-accelerating strategy. Calcium-phosphate precipitation may temporarily inhibit Ag-driven activity, but it also may cover the appearance of oxygen consumption when the product layer loses barrier continuity. Thus, a good Fe–Mn–Ag biodegradable alloy should combine controlled galvanic acceleration with distributed reactions, stable evolution of surface products, and limited oxygen depletion. The screening criterion should be the simultaneous local measurement of pH and dissolved oxygen, because the near-neutral interfacial chemistry may still be chemically challenging for tissue oxygen availability.

Conflict of interest

The author declares no conflict of interest.

References

[1] Peuster, M., Hesse, C., Schloo, T., Fink, C., Beerbaum, P., & von Schnakenburg, C. (2006). Long-term biocompatibility of a corrodible peripheral iron stent in the porcine descending aorta. Biomaterials, 27(28), 4955-4962.

[2] Moravej, M., Purnama, A., Fiset, M., Couet, J., & Mantovani, D. (2010). Electroformed pure iron as a new biomaterial for degradable stents: In vitro degradation and preliminary cell viability studies. Acta biomaterialia, 6(5), 1843-1851.

[3] Zhang, E., Chen, H., & Shen, F. (2010). Biocorrosion properties and blood and cell compatibility of pure iron as a biodegradable biomaterial. Journal of Materials Science: Materials in Medicine, 21(7), 2151-2163.

[4] Zheng, Y. F., Gu, X. N., & Witte, F. J. M. S. (2014). Biodegradable metals. Materials Science and Engineering: R: Reports, 77, 1-34.

[5] Kraus, T., Moszner, F., Fischerauer, S., Fiedler, M., Martinelli, E., Eichler, J., ... & Weinberg, A. (2014). Biodegradable Fe-based alloys for use in osteosynthesis: Outcome of an in vivo study after 52 weeks. Acta biomaterialia, 10(7), 3346-3353.

[6] Virtanen, S. (2011). Biodegradable Mg and Mg alloys: Corrosion and biocompatibility. Materials Science and Engineering: B, 176(20), 1600-1608.

[7] Witte, F. (2010). The history of biodegradable magnesium implants: a review. Acta biomaterialia, 6(5), 1680-1692.

[8] Zberg, B., Uggowitzer, P. J., & Löffler, J. F. (2009). MgZnCa glasses without clinically observable hydrogen evolution for biodegradable implants. Nature materials, 8(11), 887-891.

[9] Chen, Y., Xu, Z., Smith, C., & Sankar, J. (2014). Recent advances on the development of magnesium alloys for biodegradable implants. Acta biomaterialia, 10(11), 4561-4573.

[10] Mei, D., Lamaka, S. V., Lu, X., & Zheludkevich, M. L. (2020). Selecting medium for corrosion testing of bioabsorbable magnesium and other metals–a critical review. Corrosion science, 171, 108722.

[11] Tonna, C., Wang, C., Mei, D., Lamaka, S. V., Zheludkevich, M. L., & Buhagiar, J. (2022). Biodegradation behaviour of Fe-based alloys in Hanks' Balanced Salt Solutions: Part I. material characterisation and corrosion testing. Bioactive materials, 7, 426-440.

[12] Wang, C., Tonna, C., Mei, D., Buhagiar, J., Zheludkevich, M. L., & Lamaka, S. V. (2022). Biodegradation behaviour of Fe-based alloys in Hanks' Balanced Salt Solutions: Part II. The evolution of local pH and dissolved oxygen concentration at metal interface. Bioactive materials, 7, 412-425.

[13] Hermawan, H., Purnama, A., Dube, D., Couet, J., & Mantovani, D. (2010). Fe–Mn alloys for metallic biodegradable stents: degradation and cell viability studies. Acta biomaterialia, 6(5), 1852-1860.

[14] Schinhammer, M., Hänzi, A. C., Löffler, J. F., & Uggowitzer, P. J. (2010). Design strategy for biodegradable Fe-based alloys for medical applications. Acta biomaterialia, 6(5), 1705-1713.

[15] Čapek, J., Kubásek, J., Vojtěch, D., Jablonská, E., Lipov, J., & Ruml, T. (2016). Microstructural, mechanical, corrosion and cytotoxicity characterization of the hot forged FeMn30 (wt.%) alloy. Materials Science and Engineering: C, 58, 900-908.

[16] Schinhammer, M., Steiger, P., Moszner, F., Löffler, J. F., & Uggowitzer, P. J. (2013). Degradation performance of biodegradable FeMnC (Pd) alloys. Materials Science and Engineering: C, 33(4), 1882-1893.

[17] Čapek, J., Stehlíková, K., Michalcová, A., Msallamová, Š., & Vojtěch, D. (2016). Microstructure, mechanical and corrosion properties of biodegradable powder metallurgical Fe-2 wt% X (X= Pd, Ag and C) alloys. Materials Chemistry and Physics, 181, 501-511.

[18] Sing, N. B., Mostavan, A., Hamzah, E., Mantovani, D., & Hermawan, H. (2015). Degradation behavior of biodegradable Fe35Mn alloy stents. Journal of Biomedical Materials Research Part B: Applied Biomaterials, 103(3), 572-577.

[19] Oriňák, A., Oriňáková, R., Králová, Z. O., Turoňová, A. M., Kupková, M., Hrubovčáková, M., ... & Džunda, R. (2014). Sintered metallic foams for biodegradable bone replacement materials. Journal of Porous Materials, 21(2), 131-140.

[20] Dargusch, M. S., Dehghan-Manshadi, A., Shahbazi, M., Venezuela, J., Tran, X., Song, J., ... & Wen, C. (2019). Exploring the role of manganese on the microstructure, mechanical properties, biodegradability, and biocompatibility of porous iron-based scaffolds. ACS Biomaterials Science & Engineering, 5(4), 1686-1702.

[21] Gebert, A., Kochta, F., Voß, A., Oswald, S., Fernandez-Barcia, M., Kühn, U., & Hufenbach, J. (2018). Corrosion studies on Fe-30Mn-1C alloy in chloride-containing solutions with view to biomedical application. Materials and Corrosion, 69(2), 167-177.

[22] Sotoudehbagha, P., Sheibani, S., Khakbiz, M., Ebrahimi-Barough, S., & Hermawan, H. (2018). Novel antibacterial biodegradable Fe-Mn-Ag alloys produced by mechanical alloying. Materials Science and Engineering: C, 88, 88-94.

[23] Wiesener, M., Peters, K., Taube, A., Keller, A., Hoyer, K. P., Niendorf, T., & Grundmeier, G. (2017). Corrosion properties of bioresorbable FeMn-Ag alloys prepared by selective laser melting. Materials and Corrosion, 68(10), 1028-1036.

[24] Bagha, P. S., Khakbiz, M., Sheibani, S., & Hermawan, H. (2018). Design and characterization of nano and bimodal structured biodegradable Fe-Mn-Ag alloy with accelerated corrosion rate. Journal of Alloys and Compounds, 767, 955-965.

[25] Huang, T., Cheng, Y., & Zheng, Y. (2016). In vitro studies on silver implanted pure iron by metal vapor vacuum arc technique. Colloids and Surfaces B: Biointerfaces, 142, 20-29.

[26] Taryba, M. G., Montemor, M. F., & Lamaka, S. V. (2015). Quasi-simultaneous Mapping of Local Current Density, pH and Dissolved O2. Electroanalysis, 27(12), 2725-2730.

[27] Snihirova, D., Taryba, M., Lamaka, S. V., & Montemor, M. F. (2016). Corrosion inhibition synergies on a model Al-Cu-Mg sample studied by localized scanning electrochemical techniques. Corrosion Science, 112, 408-417.

[28] Ferreira, F., Luxardi, G., Reid, B., Ma, L., Raghunathan, V., & Zhao, M. (2020). Real-time physiological measurements of oxygen using a non-invasive self-referencing optical fiber microsensor. Nature protocols, 15(2), 207-235.

[29] Monteiro, M. C., & Koper, M. T. (2021). Measuring local pH in electrochemistry. Current opinion in electrochemistry, 25, 100649.

[30] Lamaka, S. V., Gonzalez, J., Mei, D., Feyerabend, F., Willumeit-Römer, R., & Zheludkevich, M. L. (2018). Local pH and its evolution near Mg alloy surfaces exposed to simulated body fluids. Advanced Materials Interfaces, 5(18), 1800169.